Nanoscale

PAPER

View Article Online
View Journal | View Issue

Cite this: *Nanoscale*, 2015, **7**, 659

Synthesis of functionalized 3D porous graphene using both ionic liquid and SiO_2 spheres as "spacers" for high-performance application in supercapacitors†

Tingting Li, Na Li, Jiawei Liu, Kai Cai, Mohamed F. Foda, Xiaomin Lei and Heyou Han*

In this work, a high-capacity supercapacitor material based on functionalized three-dimensional (3D) porous graphene was fabricated by low temperature hydrothermal treatment of graphene oxide (GO) using both ionic liquid (IL) and SiO_2 spheres as "spacers". In the synthesis, the introduction of dual "spacers" effectively enlarged the interspace between graphene sheets and suppressed their re-stacking. In addition, the IL also acted as a structure-directing agent playing a crucial role in inducing the formation of unique 3D architectures. Consequently, fast electron/ion transport channels were successfully constructed and numerous oxygen-containing groups on graphene sheets were effectively reserved, which had unique advantages in decreasing ion diffusion resistance and providing additional pseudocapacitance. As expected, the obtained material exhibited superior specific capacitance and rate capability compared to single "spacer" designed electrodes and simultaneously maintained excellent cycling stability. In particular, there was nearly no loss of its initial capacitance after 3000 cycles. In addition, we further assembled a symmetric two-electrode device using the material, which showed outstanding flexibility and low equivalent series resistance (ESR). More importantly, it was capable of yielding a maximum power density of about 13.3 kW kg^{-1} with an energy density of about 7.0 W h kg^{-1} at a voltage of 1.0 V in 1 M H_2SO_4 electrolyte. All these impressive results demonstrate that the material obtained by this approach is greatly promising for application in high-performance supercapacitors.

Received 19th September 2014,
Accepted 2nd November 2014

DOI: 10.1039/c4nr05473c

www.rsc.org/nanoscale

1. Introduction

Supercapacitors with high power density, excellent charging/discharging rate capability, and long life-cycles have become one of the most intensive research focuses in the electrical energy storage field.[1–4] They commonly store energy using either ion adsorption (electrochemical double layer capacitors, EDLCs) or fast surface redox reactions (pseudocapacitors).[3,5,6] It is commonly accepted that the textural properties of electrode materials play a dominant role in the development of supercapacitors. Naturally, it would be very interesting to develop a hybrid type of electrode material with unique architecture, where EDLCs and pseudocapacitors can concurrently combine to contribute to the high power properties and better energy storage performances. From this point of view, recent efforts have been focused on the preparation of high-capacity electrode materials, which may be achieved by providing desired electro-active species and by creating open porous channels with enhanced specific surface area to improve the accessibility of the ions from the electrolyte to the active regions of electrode materials.

As a promising electrode material, graphene, an atom-thick two-dimensional nanostructure, is receiving growing attention due to its excellent electronic conductivity, good electrochemical stability, high surface area and flexibility.[4,7,8] Various morphologies of graphene or graphene-based composites have been developed as electrode materials for supercapacitors.[9–15] Nevertheless, easy and efficient reduction of graphene oxide (GO) to reduced graphene oxide (rGO) is still a key topic in this research field. Among all the reduction strategies, thermal exfoliation of GO is conceived to be simple and environmentally friendly, in which no hazardous reductant is used. But this process usually requires a rapid heating (>2000 °C min^{-1}) up to high temperature, which means large energy consumption and critical treatment conditions.[16] Recently, hydro-

State Key Laboratory of Agricultural Microbiology, College of Science, College of Food Science and Technology, Huazhong Agricultural University, 1 Shizishan Street, Wuhan 430070, PR China. E-mail: hyhan@mail.hzau.edu.cn; Fax: +86-27-87288505; Tel: +86-27-87288505

†Electronic supplementary information (ESI) available. See DOI: 10.1039/c4nr05473c

thermal treatment of GO has attracted more and more attention because of its outstanding advantages such as high yield, simple manipulation, easy control, and environmentally friendliness.[17–19] Particularly, low temperature hydrothermal treatment can maintain desired oxygen-containing groups on the surface of graphene, which not only enhances the surface wettability of graphene electrodes but also significantly increases the specific capacitance by the faradaic reaction occurring during the electrochemical charge–discharge process.[11,19] Inevitably, the strong interlayer van der Waals force often causes irreversible sheet-to-sheet re-stacking in the thermal reduction process, resulting in the deterioration of effective surface area and subsequent decrease of the specific capacitance. Consequently, considering practical applications, the graphene materials with ideal porous nanostructures as well as high surface area are urgently desirable and of great potential, in particular for supercapacitors.

For this purpose, researchers tend to incorporate a "spacer" between graphene layers[13,20,21] or fabricate wrinkled/porous graphene sheets.[8,11,22–24] For example, cyanamide was introduced to GO layers to develop crumpled nitrogen-doped graphene nanosheets (C-NGNSs) with a pore volume as high as 3.42 $cm^3\ g^{-1}$, and they exhibited high capacity, excellent rate capability, and long-term stability as an electrode for supercapacitors.[25] Meng *et al.* developed a 3D-RGO film using $CaCO_3$ as a sacrificial template, which showed low equivalent series resistance (ESR) and excellent cycling stability (90% capacitance retention over 5000 cycles at 5 A g^{-1}).[14] Hollow PPy spheres were also inserted between rGO layers and they delivered an amazing specific capacitance over 500 F g^{-1} at a current density of 5 A g^{-1} even after 10 000 cycles.[6] In addition to the abovementioned, even water can also be used as spacer material.[26] The unique porous structures or porous sheets can greatly improve the accessibility of the electrolyte to the surface of the electrode and effectively promote charge transport. It is also noteworthy that three-dimensional (3D) graphene materials can better meet the need for high-performance electrodes, because they not only possess the intrinsic properties of two-dimensional graphene sheets, but also additionally provide attractive characteristics for improvement of the performance of supercapacitors. Particularly, the 3D graphene with unique porous architecture is beneficial for electrolyte access and can significantly improve the utilization of the active materials decorated on these electrically conductive channels, which enhance the performances of both EDLCs and pseudocapacitors. Although introducing a "spacer" to assemble graphene into randomly arranged 3D porous nanostructures is regarded to be an effective strategy for increasing their electrochemical performances, some still have either unsatisfactory surface area[11,27,28] or limited porous channel distribution.[29–31] These unsatisfactory characteristics inevitably result in serious internal resistance and extremely significant capacitance degradation, particularly at high charge–discharge rates. Thus, to further improve the rate capability, developing generalized methods to prepare 3D hierarchical porous graphene with high surface area are critical.

Herein, we demonstrated a unique functionalized 3D porous graphene (denoted as PrGO-IL) that was prepared by facile low temperature hydrothermal treatment of GO using both ionic liquid (IL) and SiO_2 spheres as "spacers". Introduction of dual "spacers" can easily produce hierarchical porous structure, at the same time high surface area was obtained for graphene. Compared with rGO-IL, only using IL as a "spacer", the PrGO-IL electrode displayed higher specific capacitance and rate capability while maintaining excellent cycle performance. Furthermore, a symmetrical two-electrode configuration also was assembled, which achieved outstanding features, including superior flexibility, high power density and low ESR. The superior electrochemical performances of PrGO-IL can be attributed to the synergistic effects of IL, oxygen-containing groups, and unique 3D porous architecture. Firstly, IL features nonvolatility, excellent thermal stability, wide electrochemical stability windows, good ion conductivity and solubility,[32] which can not only assist reduction of GO, but also play a key role in controlling the assembly of graphene sheets into 3D structures. Secondly, the reserved large amounts of stable oxygen-containing groups on graphene sheet by low temperature hydrothermal treatment of GO have enormous contribution to the capacitance increase by improving the wetting properties and providing additional pseudocapacitance. Thirdly, 3D graphene with hierarchical porous structure accelerates the rate of ion transfer and reduces the inner resistance of the electrodes, leading to a sufficient utilization of graphene surface even at high rates.

2. Experimental section

2.1. Chemicals

Natural graphite powder (99.99%), tetraethoxysilane (TEOS, ≥99.0%) and poly (diallyldimethylammonium chloride) (PDDA, 20 wt%) were purchased from Sigma-Aldrich. $K_2S_2O_4$, P_2O_5, absolute ethanol and $KMnO_4$ with analytical grade and 98% H_2SO_4, 30% H_2O_2, 36% HCl, $NH_3{\cdot}H_2O$ (25%–28%), and HF (≥40%) aqueous solution were purchased from Shanghai Chemical Reagents Company. 1-Butyl-3-methylimidazolium chloride ([BMIm]Cl, >99%) was from the Lanzhou institute of chemical physics. All the reagents were used directly without further purification.

2.2. Synthesis of PDDA modified SiO_2 spheres (*p*-SiO_2)

SiO_2 spheres were synthesized following a slightly modified Stöber process. In a typical synthesis, 3.15 mL of ammonium aqueous solution was rapidly added into a mixture of 75 mL of ethanol, 10 mL of distilled water, and 6 mL of TEOS and then stirred at room temperature for 1.5 h. The SiO_2 spheres were centrifugally separated from the suspension and washed with distilled water and ethanol. The freshly prepared SiO_2 spheres were functionalized with PDDA to obtain surface positive charges. First, 0.1 g dry SiO_2 spheres were dispersed into 20 mL distilled water by ultrasonication. Then the resulting dispersion was added to PDDA solution (20 mg dissolved in

5 mL distilled water) and stirred for 30 min at room temperature. Free PDDA was removed by three cycles of centrifugation/washing/redispersion. Finally, as-synthesized p-SiO_2 was dispersed into distilled water with the total volume of 10 mL to form a homogeneous suspension.

2.3. Synthesis of functionalized 3D porous graphene nanostructure (PrGO-IL)

Graphene oxide (GO) nanosheets were prepared with a modified Hummers method (ESI†).[33] In a typical experiment, the as-prepared graphite oxide powder (16 mg) was dispersed in 20 mL of distilled water to undergo the exfoliation *via* sonication for 2 h. Then the GO suspension was added to the abovementioned p-SiO_2 solution and gently stirred for 1 h at room temperature. After that, the IL solution (1.7448 g dissolved in 5 mL distilled water) was further added and stirred for a while. Subsequently, entire reaction solution was transferred to a Teflon autoclave and treated at 160 °C for 12 h. After cooling naturally to room temperature, the solid precipitate was collected by filtration, and then freeze-dried to obtain rGO-IL/SiO_2 spheres composites. Subsequently, the composites was treated with HF aqueous solution for 24 h, followed by centrifugation and washed with distilled water. Finally, the PrGO-IL was obtained by freeze-drying. For comparison, pure rGO was prepared using the same method with the exception of p-SiO_2 and IL. Similarly, rGO-IL and PrGO were also obtained with the same procedure without adding p-SiO_2 and IL, respectively.

2.4. Characterization

Scanning electron microscopy (SEM) images were taken by a JEOL JSM-6700F field emission scanning electron microscope. Transmission electron microscopy (TEM) images were obtained using a JEM-2010 with the microscope operating at 200 kV. X-ray diffraction (XRD) spectra were obtained using a Rigaku D/MAX-rA diffractometer with Cu Kα radiation (λ = 1.5406 Å). Raman spectra were recorded by a Renishaw inVia Raman spectrometer equipped with a He–Ne laser excitation source operating at 632.8 nm. Infrared spectra were collected on a Nicolet Avatar-330 Fourier transform infrared (FTIR) spectrometer with 2 cm^{-1} resolution using the KBr pellet technique. Thermal gravimetric analysis (TGA) measurements were examined using a NETZSH TG 209C thermobalance with a heating rate of 10 °C min^{-1} under N_2. The dynamic light scattering (DLS) data of SiO_2 was acquired using a Malvern Zetasizer Nanoseries using 633 nm laser at 25 °C. X-ray photoelectron spectra (XPS) were measured by a Thermo VG Multilab 2000 spectrometer equipped with a monochromatic Al Kα radiation source at room temperature. Elemental analyses were performed with an Elementar Vario Micro-cube elemental analyzer. The surface area of the as-synthesized product was measured by the Brunauer–Emmett–Teller (BET) method with the adsorption data at the relative pressure (P/P_0) range of 0.05–0.35 using nitrogen adsorption and desorption isotherms by an Autosorb-1 from Quantachrome Instruments. The total pore volumes were estimated at P/P_0 = 0.99. The pore size distribution plot was obtained by the Barrett–Joyner–Halenda (BJH) method.

2.5. Electrochemical measurements

The working electrode was prepared by mixing an active material (80 wt%) with carbon black (10 wt%) and polytetrafluoroethylene (PTFE, 10 wt%) in isopropanol. The slurry of the mixture was rolled to a thickness of ~100 μm and left to dry in an oven at 80 °C for 24 h. Then, the film was cut into a suitable shape (8 mm × 8 mm) and pressed on stainless steel mesh under 6 MPa, which was used as the current collector. The typical mass loading on one electrode was between 2 and 4 mg. The electrochemical measurement was carried out using both a three-electrode and two-electrode configuration, with 1 M H_2SO_4 as electrolyte. In a three-electrode configuration, besides the working electrode, a Ag/AgCl reference electrode and a platinum foil counter electrode were used in the measurement. However, the symmetrical two-electrode configuration consisted of two symmetric working electrodes, which were assembled together with one piece of cellulose paper separator sandwiched in between. A stainless steel mesh was used as the current collector and the entire configuration was sealed by PET membrane. All the electrochemical measurements were carried out with a CHI 660D (Chenhua, Shanghai) electrochemical workstation.

Cyclic voltammetry (CV), galvanostatic charge–discharge (GCD) and electrochemical impedance spectroscopy (EIS) were employed to evaluate the electrochemical performances of electrodes. The gravimetric specific capacitance for the three-electrode cell was obtained from the GCD curves as: $C_g = I \times t/V$, where C_g is the specific gravimetric capacitance (F g^{-1}), I is the current density (A g^{-1}), t is the discharge time (s), and V (V) is the discharge voltage range.[12,34] For the two-electrode system, the total capacitance of the supercapacitor was calculated from the galvanostatic discharge process according to the following equation: C_{total} (F g^{-1}) = $I \times t/(m \times V)$, where I (A), t (s), V (V) and m (g) are the discharge current, the discharge time, the operation potential window excluding the IR drop during the discharge process and the total mass of two electrodes, respectively. The specific capacitance of the single electrode is thus calculated as $C_{single} = 4 \times C_{total}$. The energy density ($E$) and the power density (P) were calculated based on the following equations: $E = 1/2C_{total}V^2$, $P = E/t$, where C_{total} is the total capacitance of symmetric configuration according to the GCD curves (F g^{-1}), V is the voltage scan range (V) and t is the discharge time (s).[24,35] The EIS measurement of the supercapacitor was performed with an amplitude of 5 mV in the frequency ranges of 10 mHz–100 kHz.

3. Results and discussion

3.1. Characteristics of the samples

The procedure for synthesizing PrGO-IL is schematically illustrated in Scheme 1. The silica nanospheres with particle size around 250 nm were first prepared by the well-known Stöber

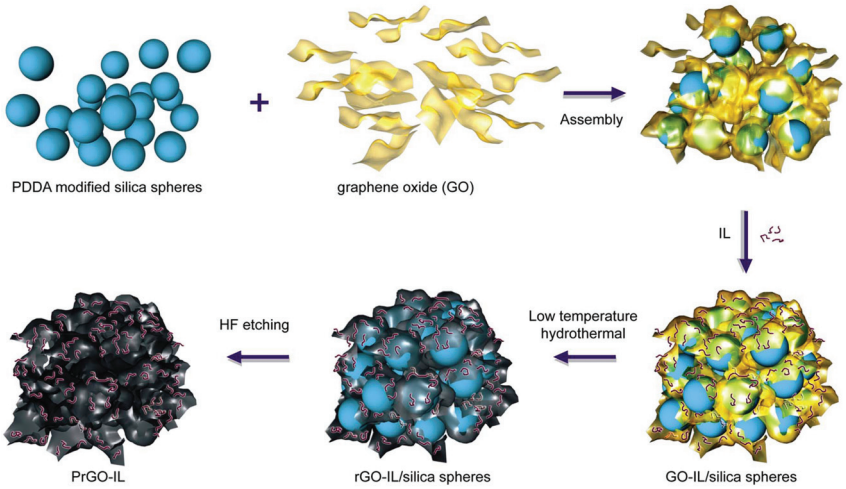

Scheme 1 Schematic illustration of the synthesis of PrGO-IL.

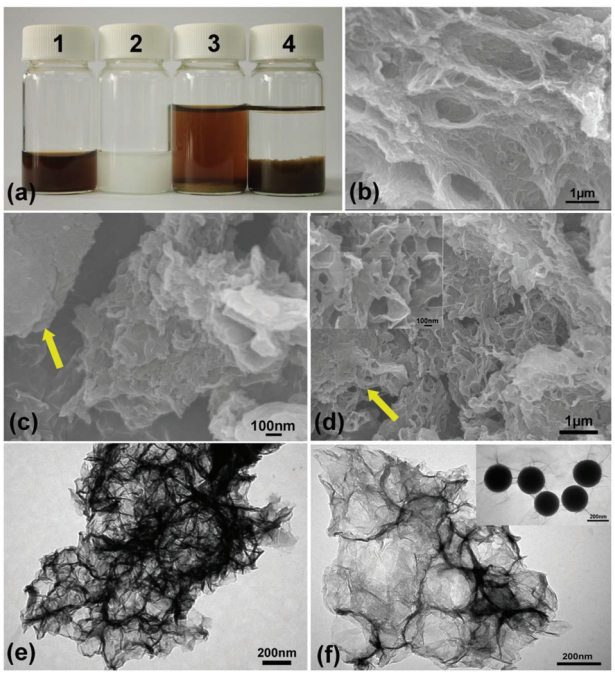

Fig. 1 (a) Digital images of GO, *p*-SiO_2 suspension, GO/silica spheres composites and GO-IL/silica spheres composites. SEM images of (b) rGO-IL, (c) PrGO and (d) PrGO-IL (inset: the enlarge SEM image of PrGO-IL). TEM images of (e) rGO-IL and (f) PrGO-IL (inset: the TEM image of GO-IL/silica spheres composites).

method (Fig. S1, ESI†). They were then modified with PDDA by electrostatic interactions. Subsequently, the resulting positively charged *p*-SiO_2 (Fig. 1a-2) was self-assembled with GO sheets (Fig. 1a-1), resulting in a GO/silica spheres composite (Fig. 1a-3). Once the IL was added, the composites stacked immediately, which was driven by the hydrophobic and π–π stacking interactions of the conjugated structures of IL-modified GO.[9] During this process, the IL can occupy the remaining negative charge of GO sheets and simultaneously *p*-SiO_2 spheres were wrapped in-between GO sheets as "spacer" to form an interesting sandwiched nanostructure that effectively prevents the graphene sheets from severe agglomeration. It is noted that the IL as another "spacer" anchored on the graphene increases the distance between the graphene sheets and also prevents the formation of a densely stacked structure. The as-prepared GO-IL/silica sphere composites (Fig. 1a-4) were then sealed in a Teflon-lined autoclave and maintained at 160 °C for 12 h to reduce GO into rGO. The final products were obtained by removing the silica skeleton and subsequent freeze drying. Notably, the residual PDDA after etching SiO_2 spheres can still attach to the graphene surface, which also contributes to the prevention of the re-stacking of graphene in the subsequent processing. For comparison, we also prepared pure rGO, rGO-IL and PrGO as electrode materials for supercapacitors.

SEM and TEM images show that rGO exhibits the typical nanosheet structure of graphene with less severe stacking (Fig. S2, ESI†). Fortunately, the rGO still could be easily dispersed in the water without any precipitation as residual oxygen-containing groups remained on the graphene surface (inset of Fig. S2a†), indicating a mild reduction. In the case of the rGO-IL sample, the SEM image reveals a randomly distributed and loosely stacked structure (Fig. 1b). The corresponding TEM image is presented in Fig. 1e. Cabbage leaves-like graphene with a relatively curved and wrinkled structure was created after IL assisted hydrothermal reaction. The crumples can contribute to resist the re-stacking of overlapped graphene to keep the large surface area and supply a fast ion transport channel for application in supercapacitor.[11,25] Interestingly, in PrGO hybrid architectures (Fig. 1c), partial GO sheets wrapped *p*-SiO_2 crumpled to minimize their surface energies, forming wrinkled surface. The remaining GO dispersed in the supernatant (Fig. 1a-3) tend to face-to-face stack during low temperature hydrothermal process, resulting in a relatively smooth surface (yellow arrow pointing), which is quite unfavorable for increased surface area. In contrast, for PrGO-IL, when *p*-SiO_2

was introduced into the composites, they were completely encapsulated in GO sheets with the assistance of IL (inset of Fig. 1f). This resulted in a clean and transparent solution, and no separated GO sheets or other additives existing in supernatant, indicating an efficient embedding, as depicted in Fig. 1a-4. Compared with rGO-IL, the SEM image of PrGO-IL shows the porous structure throughout the entire inter-layer of graphene, which is marked by the yellow arrow (Fig. 1d), demonstrating the important role of SiO_2 spheres as "spacers" in preventing the re-stacking of graphene sheets. These pores can be clearly observed from the magnified SEM image (inset of Fig. 1d). In addition, the evident traces of SiO_2 "spacer" on the surface of graphene sheets are further confirmed by TEM observation (Fig. 1f), which intuitively indicates that the pore size is close to the diameter of the SiO_2 spheres. Therefore, the morphology of pores could easily be tuned by choosing different sacrificial "spacers", indicating the feasibility and universality of our method. The abovementioned results also proved that freeze-drying process could well maintain the 3D microstructures.

It is interesting to note that the vertically aligned graphene sheets with both slight wrinkles and open structures are observed for both rGO-IL and PrGO-IL (Fig. 2a and b), which are produced by the structure-directing role of IL. These vertical open inter-sheet channels can provide a large number of exposed graphene edges as contact points, and thus further increase redox active sites during charging and discharging. Compared with rGO-IL, the graphene sheets of PrGO-IL arrange more loosely and the larger space between the sheets is beneficial for fast ion transport. Consequently, the electrons can also be more efficiently transferred along the graphene plane.[36,37] Moreover, the nitrogen adsorption–desorption isotherms of rGO-IL and PrGO-IL shown in Fig. S3, ESI† reveal distinct hysteresis loops, confirming their porous structure.[29] Particularly, a steep increase of nitrogen absorption of PrGO-IL at a high relative pressure (P/P_0 = 0.85–0.99) reveals the presence of a large number of macropores. As expected, the BET specific surface area of PrGO-IL was calculated to be 341 $m^2\ g^{-1}$ and is considerably higher than that of rGO-IL (172 $m^2\ g^{-1}$). Large surface area can greatly enhance the electrode–electrolyte interface and it is also beneficial for electrolyte access. In addition, the total pore volumes for rGO-IL and PrGO-IL are about 1.1 $cm^3\ g^{-1}$ and 1.8 $cm^3\ g^{-1}$, respectively. The higher pore volume of PrGO-IL is extremely favorable for providing rich sites to adsorb ions and accelerating electron transfer.[25] The abovementioned results also clearly reveal that the SiO_2 spheres effectively prevent the re-stacking/agglomeration of graphene sheets as "spacers". In addition, the hierarchical pore size distribution (PSD) together with meso- and macroporous features can be obtained (inset of Fig. S3, ESI†), which is partly generated from IL induced self-assembly with the wrinkled and folded domains. The rest is probably derived from the left space of encapsulated water after the freeze-dried process. Notably, the formation of a large proportion of spherical macropores is mainly attributed to the presence of SiO_2 spheres. The hierarchical porous architecture is favorable for rapid ion diffusion and intense charge storage/release.[15]

XRD patterns of the GO, rGO, rGO-IL, PrGO and PrGO-IL are shown in Fig. 3a. The as prepared GO exhibits an intense peak centered at $2\theta = 11°$ (001), corresponding to the interlayer distance of 0.80 nm. After low temperature hydrothermal reduction, the peak disappeared along with the appearance of two new peaks around 2θ = 24.5° (002) and 43.5° (100), suggesting the successful reduction of GO.[22] The broad (002) reflection indicates the poor ordering of graphene sheets along their stacking direction,[18] which is consistent with the SEM results. In addition, the peaks shifts slightly lower than that of chemically reduced graphene,[7,38] which can be ascribed to both the existence of the residual oxygenated functional groups on the rGO sheets and the introduction of spacer materials between the graphene layers.[7,25]

The abovementioned observation was also supported by Raman measurements. As shown in Fig. 3b, each of the Raman spectra exhibits two remarkable bands. The D band at around 1330 cm^{-1} is associated with the structural defects or partially disordered structures of graphitic domains, whereas the G band at about 1590 cm^{-1} corresponds to the ordered sp^2 bonded carbon.[6,39] The I_D/I_G values of GO, rGO, rGO-IL, PrGO and PrGO-IL were calculated to be 0.93, 1.15, 1.10, 1.05 and 1.08, respectively. The D/G intensity ratio increases slightly, which not only suggests the presence of defects, wrinkles, or ripples on graphene after low temperature hydrothermal reduction, but also indicates mild reduction.[36,40] As seen from the curve of PrGO-IL, the 2D-band centered at around 2650 cm^{-1} with a broader expansion indicates the presence of

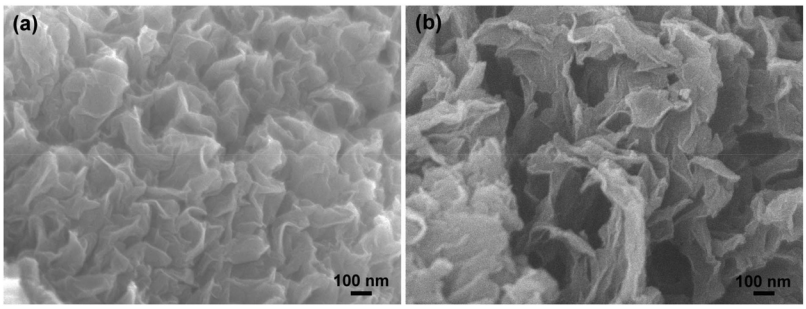

Fig. 2 The magnified SEM images of (a) rGO-IL and (b) PrGO-IL.

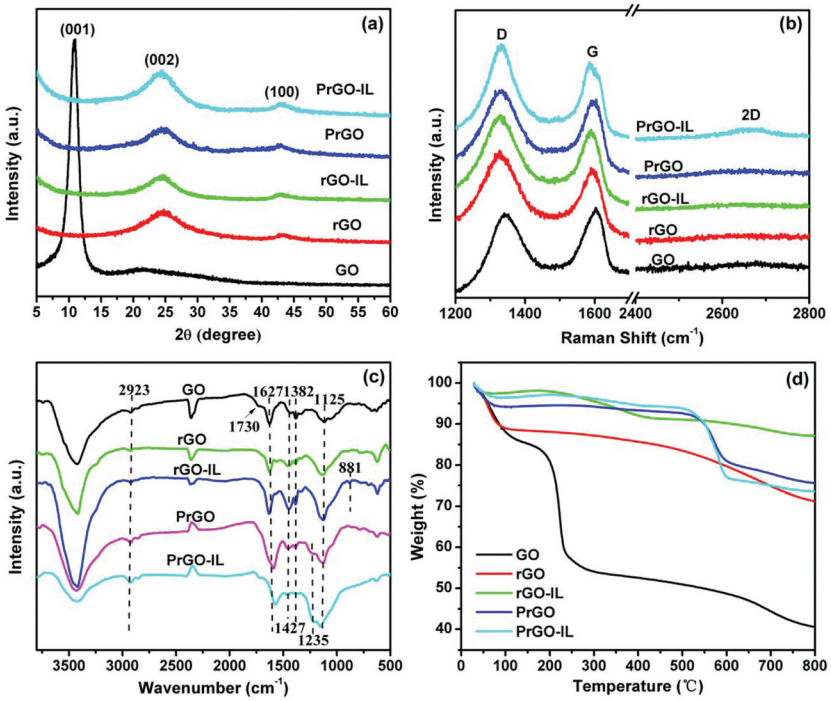

Fig. 3 (a) XRD patterns (b) Raman spectra and (c) FTIR spectra of as-synthesized GO, rGO, rGO-IL, PrGO, and PrGO-IL. (d) TGA curves of all samples at a heating rate of 10 °C min^{-1} under a nitrogen atmosphere.

loosely stacked graphene layers due to the intercalation of SiO_2 spheres "spacer".[41]

Further comparative characterization of GO before and after low temperature hydrothermal reduction was carried out with FTIR spectroscopy. As shown in Fig. 3c, the IR spectrum of GO shows evidence of hydroxyl groups on the surface (O–H at ~3422 and ~1382 cm^{-1}), and clearly, the observed peaks at 1627 cm^{-1}, 1125 cm^{-1}, 1427 cm^{-1}, 2923 cm^{-1} and 1730 cm^{-1} are assignable to the characteristic C=C conjugation band, alkoxy C–O stretch, carboxy C–O stretch, C–H stretch and a strong C=O stretch, respectively.[42,43] Note that the spectra after reduction change slightly except for the bands at 1730 cm^{-1} for the C=O stretch are found to vanish and the bands at 1382 cm^{-1} for O–H stretch are attenuated. The obtained results are similar to that of electrochemical reduction,[44] which suggests slight deoxygenation by the mild reduction process. Moreover, decoration of graphene with IL is reflected by the appearance of a weak peak at 881 cm^{-1} of rGO-IL, attributable to the C–N bonds of adsorbed IL.[19,45] In particular, an additional peak corresponding to the stretching vibration of the C–F covalent bonds is also observed at 1235 cm^{-1} for PrGO and PrGO-IL, which is probably because fluorine is easily grafted onto the basal plane of graphene during SiO_2 etching process.[46,47] This result is also confirmed by XPS measurements (Fig. S4, ESI†), in which the weak peaks of fluorine can be clearly seen.

XPS was performed to evaluate the chemical composition of the as-prepared samples. The high-resolution C 1s spectrum of GO can be fitted into four peaks centered at about 284.8, 286.2, 287.3 and 288.8 eV (Fig. S4b, ESI†), corresponding to C–C, C–O, –C=O and –O–C=O groups.[7,29,48,49] However, after the samples experienced low temperature hydrothermal treatment (Fig. S4c–f, ESI†), the oxygen content decreased evidently, particularly the –C=O, well consistent with the FTIR spectra. The above observed variation is also evidenced by a significantly increased C/O ratio after the occurrence of reduction (Table S1, ESI†). In addition, elemental analysis reveals that the rGO-IL has the highest nitrogen content of 2.50 wt%, indicating the successful attachment of IL on the surface of graphene sheets. It's N 1s XPS spectrum (Fig. S5a, ESI†) shows a pronounced peak located at 401.2 eV, which is indicative of the effective connection of imidazolium ions to the graphene.[49,50] Moreover, the N 1s XPS spectra of PrGO and PrGO-IL were also observed (Fig. S5b and c, ESI†). The former reflects two peaks at 402.5 and 399.7 eV, corresponding to the charged nitrogen and uncharged nitrogen forms of adsorbed PDDA, respectively.[45,51] In the latter case, the additional peak located in the middle is credited to the characteristic of IL. Due to the strong binding of IL with graphene, partial positive charge of PDDA cannot interact with graphene; therefore, the intensity ratio of charged and uncharged nitrogen of PrGO-IL sample is substantially higher than that of PrGO. However, PrGO and PrGO-IL show lower nitrogen content contrary to what is observed for rGO-IL, indicating that a relatively small number of PDDA (and IL) is attached on graphene surface.

TGA was further conducted to investigate the thermal stability (Fig. 3d). It can be seen that all the samples show different mass losses below 100 °C due to the elimination of adsorbed

water. In the case of GO, a significant weight loss from 200 to 250 °C occurs mainly due to the decomposition of the labile oxygen functional groups.[7] In contrast, no evident weight loss occurred for reductive samples at the same temperature range, demonstrating that the remaining oxygen-containing functionalities are stable. The recorded plot of rGO-IL displays an andante weight loss between 250 °C and 400 °C, ascribed to the decomposition of IL in the interlayer of graphene. A similar decomposed stage is observed for PrGO-IL, indicating the existence of IL between graphene sheets. For PrGO and PrGO-IL, the weight losses occur below 600 °C due to the decomposition of attached PDDA (and IL), as well as the detachment of unstable heteroatoms.[45,49] Nevertheless, the significant degradation process approaching 600 °C is most probably related to the removal of unstable fluorine atoms.[52]

3.2. Electrochemical performance study

The electrochemical characteristics of the prepared electrode materials were initially investigated using a three-electrode system in aqueous 1 M H_2SO_4 electrolyte (Fig. 4). CV collected from rGO-IL, PrGO and PrGO-IL exhibit quasi-rectangular curves, but a significantly distorted curve was obtained from rGO (Fig. 4a), indicating poor capacitive behavior of the rGO electrode. In addition, one pair of redox waves can be clearly seen from the CV curves, which is also observed from the rGO electrode at a low scan rate (Fig. S6a, ESI†). This is mainly attributed to the redox reaction of the remaining high level of surface oxygen functional groups (above 20 wt% based on elementary analysis). The CV curves demonstrate that the capacitance of the active materials is derived from the pseudocapacitance together with the EDLCs produced at the electrode–electrolyte interface. Significantly, in comparison to rGO and PrGO, the rGO-IL and PrGO-IL exhibit considerably higher current density (Fig. 4a), symbolizing a higher capacitance value. Such inferior electrochemical behavior of rGO and PrGO is related to their densely packed layered structure, which would kinetically limit the electrolyte ions from penetrating into the graphene planes. While GO sheets might be partially adsorbed on the *p*-SiO_2 spheres by electrostatic ion interactions in the initial stage, some would detach from *p*-SiO_2 spheres with the constant disappearance of oxygen-containing groups in the subsequent hydrothermal treatment; therefore, PrGO shows severe agglomeration of graphene sheets, which is similar to that observed in rGO. Consequently, the decrease in exposed surface leads to inferior specific capacity and rate capability. Therefore, the introduction of IL "spacers" play an essential role in promoting the electrochemical performance of rGO-IL and PrGO-IL composites, which not only induce synthesis of 3D porous graphene with optimized structure, but also serve as electrically conductive channels to improve the electron transport performance of coated graphene sheets.[9]

Similar to the CV results, the significant redox contribution also caused a distortion of the GCD curves, as shown in Fig. 4b. The rGO electrode demonstrates significant IR drop upon discharge, indicating a high internal resistance. Calculated by the GCD curves recorded at 2.0 A g^{-1}, the capacitances of rGO, rGO-IL, PrGO and PrGO-IL are 134, 200, 175 and 242 F g^{-1}, respectively. PrGO-IL presents the highest capacitance value, which is substantially larger than that of previously reported graphene composite electrodes, such as 201.5 F g^{-1} of CNT-HCS,[53] 229 F g^{-1} of RGO-PPy and 104 F g^{-1} of RGO-PEDOT[35] at 0.5 A g^{-1}, as well as considerably larger than that of

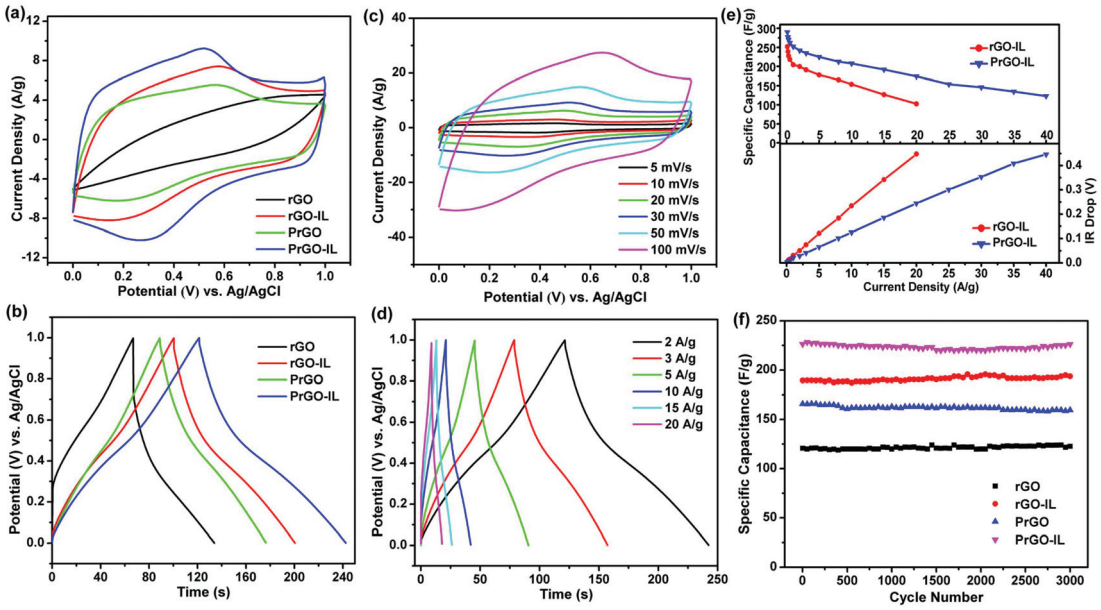

Fig. 4 Electrochemical performance of as-prepared electrode materials in a three-electrode setup. (a) CV curves at the scan rate of 30 mV s^{-1}, and (b) GCD curves at the current density of 2 A g^{-1}. (c) CV profiles of PrGO-IL at different scan rates, and (d) GCD curves of PrGO-IL at different current densities. (e) Variation of specific capacitance and IR drops of rGO and PrGO-IL against current density, and (f) cycle performance of the electrode materials in aqueous 1 M H_2SO_4 measured at 4 A g^{-1}.

surfactant-stabilized graphene (116–194 F g^{-1}) at 1 A g^{-1}.[12] The high specific capacitance of the PrGO-IL electrode can be attributed to the greatly improved surface area with hierarchical porous channels and ample oxygen-containing functionalities while guaranteeing the contribution of EDLCs and pseudocapacitance to the total capacity.

We further proceeded to investigate the rate-dependent CVs for rGO-IL and PrGO-IL over a scan rates range of 5–100 mV s^{-1} (Fig.4c and S6b, ESI†). It is evident that the oxidation peaks and reduction peaks shift to a more positive position and a more negative position with increasing scan rate, respectively. This is due to an increase of the internal diffusion resistance within the pseudoactive material.[54] Compared with PrGO-IL, the shapes of the CV curves for rGO-IL are more evidently distorted as the scan rate increased to a relatively high level. The larger specific surface area and pore volumes of PrGO-IL supply numerous electroactive surface sites for better electrolytic contact, resulting in the higher charge storage capacity compared to rGO-IL. To evaluate the potential application of the PrGO-IL electrode for supercapacitors, GCD measurements were carried out at various current densities ranging from 2 A g^{-1} to 20 A g^{-1} (Fig. 4d). Moreover, the GCD curves are presented for comparison for rGO-IL electrode (Fig. S6c, ESI†). Evidently, upon increasing the current density to 10 A g^{-1}, the GCD curves deviate slightly from the ideal shape for rGO-IL, while PrGO-IL still maintains well as current density up to 20 A g^{-1}, and these prove the quick charge propagation capability of PrGO-IL. Undoubtedly, the introduction of SiO_2 spheres as "spacers" plays an important role in the increase of the electroactive surface area and the enhancing of the electron transfer kinetics. As described in Fig. 4e, the specific capacitance of PrGO-IL decreases slightly with the increase of charge/discharge rates, additionally, suggesting better rate capability of the PrGO-IL electrode than the rGO-IL. The relatively smaller IR drops at same current densities, further confirming its lower internal resistance. On the basis of a series of comparative experiments, it can be concluded that the created macropores between graphene sheets are a key factor in maintaining the high rate performance, which afford efficient pathways for electrolyte transport. Simultaneously, these macropores act as ion buffering reservoirs, which can minimize the diffusion distances to the interior surfaces. As expected, for PrGO-IL, a high specific capacitance value of 262 F g^{-1} at current density of 0.5 A g^{-1} was obtained. Most importantly, as the current density was increased to 20 A g^{-1}, the capacitance still preserved a high value of 175 F g^{-1}. The excellent rate capability is of vital importance to supercapacitors in power applications. The significantly improved capacitance and rate-capability of PrGO-IL can be ascribed to the unique 3D porous architecture with large surface area and high electrical conductivity, which promoted ion transport and electron migration, as well as increased the electrochemically active sites. Taking into account the differences in the preparation processes, these results highlight the significant role of dual "spacers" in dramatically promoting the kinetic diffusion of electrolyte in the interior of electrode.

Fig. 4f shows the cycling performance of the electrode materials in 1 M H_2SO_4 electrolyte at a current density of 4.0 A g^{-1}. As displayed, no evident capacitance losses are observed for all the electrodes even after 3000 cycles, revealing good long-term cyclic performance. The excellent stability with high capacitance of PrGO-IL can be attributed to its good mechanical stability and conductivity, as well as the distinctive 3D porous structure. It also proved that introducing "spacers" could not affect the electrochemical stability. Therefore, the high-rate performance of PrGO-IL electrode with superior cycling stability is suitable for application in supercapacitors.

The supercapacitor performances of the PrGO-IL were then investigated by a symmetrical two-electrode system in 1.0 M H_2SO_4 electrolyte. Fig. 5a presents the scan rate-dependent CVs for PrGO-IL over a scan rate range of 10–200 mV s^{-1}, with a potential window of 0–1.0 V. The small 'humps' in the CV curves near 0 V are attributable to pseudocapacitance based on faradaic reactions. It is seen that the PrGO-IL manifests an enhanced area of CV curve with increasing scan rate and a nearly rectangular shape is retained even at the scan rate of 200 mV s^{-1}. The GCD curves at different current densities shown in Fig. 5b reveal that all of the charging curves are symmetrical with their corresponding discharge counterparts, indicating good capacitive behavior. The deviation from the ideal linearity of GCD curves is also caused by the retention of oxygen containing groups on graphene surface.[55] The difference in the shapes of CV and GCD curves for the two- *versus* the three-electrode setup is related to a function of voltage. In the three-electrode setup the entire potential window is applied to the working electrode, whereas in a symmetrical configuration the potential window is shared between the two electrodes.[56] Consequently, the integral redox peaks were clearly observed from CV curves when the voltage range enlarged from −1.0 to 1.0 V (Fig. S7a, ESI†). The similar pseudocapacitive behavior is also confirmed by GCD curves, as shown in Fig. S7b, ESI,† which exhibit notable curvatures of the slopes.

In addition, symmetrical two-electrode devices for rGO-IL were also assembled and analyzed with the same procedures. The CV and GCD curves are presented in Fig. S7c and d, ESI.† With increasing scan rate, distorted CV curves of rGO-IL are observed. Moreover, the galvanostatic discharge time is significantly shorter than that of the PrGO-IL sample at the same current density, indicating lower capacity than PrGO-IL, similar to what was observed in the three-electrode system. Impressively, at a current density of 2.0 A g^{-1}, the specific capacitance of PrGO-IL supercapacitor is 206 F g^{-1} (based on the single electrode), which is greatly higher than that for rGO-IL (138 F g^{-1}). It is also considerably higher than that recently reported for graphene paper,[55] DEG/graphene composite[21] and 3D-RGO film[14] supercapacitors in aqueous electrolyte. Notably, the capacitance shows a slight decrease to 185 F g^{-1} even at a current density of 15 A g^{-1}, whereas the rGO-IL only shows a capacity of 84 F g^{-1} at the same current density, illustrating an excellent rate capability for PrGO-IL-based supercapacitors. The dramatic performance improvement after

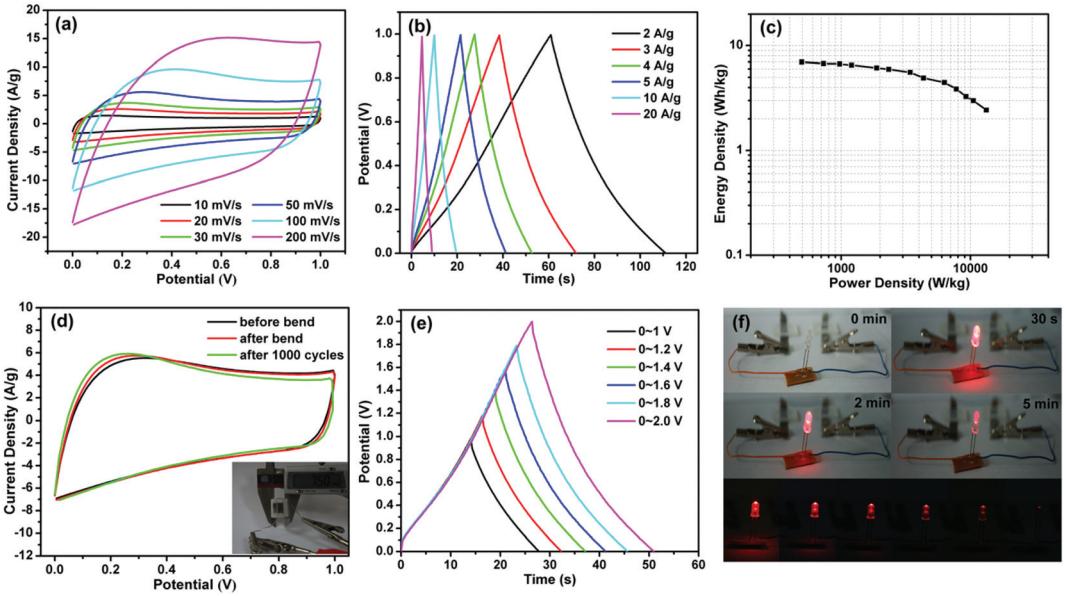

Fig. 5 Electrochemical performance of assembled two-electrode capacitor with PrGO-IL as symmetric electrode and 1.0 M H_2SO_4 as aqueous electrolyte. (a) CV profiles at different scan rates, and (b) GCD curves at different current densities. (c) Ragone plot collected at different current densities, and (d) CV curves tested under bending conditions with a scan rate of 50 mV s^{-1} (Inset: digital image of a bending device). (e) GCD curves collected at current density of 4 A g^{-1} for two tandem devices, and (f) Brightness variations of the LED powered by two tandem devices with a working potential of 1.5 V.

SiO_2 spheres introduction can first be attributed to the smaller internal resistance of the PrGO-IL electrode as compared to the rGO-IL in the EIS (Fig. S8, ESI†). A smaller semicircle radius at high frequency and more vertical curve at low frequency region are observed for PrGO-IL, representing the smaller charge transfer resistance (R_{ct}) and kinetic diffusion resistance.[5,10,34,36] R_{ct} of the sample from rGO-IL (3.25 Ω) is however greater than that of PrGO-IL (0.97 Ω). The reduced R_{ct} of PrGO-IL is consistent with its comparatively good electrical conductivity. At very high frequencies, the intercept at the real axis represents the ESR. rGO-IL has a higher ESR value (1.35 Ω) compared with PrGO-IL (1.03 Ω), further demonstrating the improved charge transport properties of PrGO-IL. In addition, the increased specific surface area and pore volume of PrGO-IL can ensure the fine contact of electrolyte ions with graphene sheets, leading to the maximum utilization of surface active sites during the electrochemical reactions. Finally, the diffusion/transport of electrolyte ions can be improved by the introduction of open hierarchical porous channels, together with the improved accessibility of electrolytes to electrodes resulting from the existence of hydrophilic oxygen-containing functional group. The abovementioned factors acting synergistically endow the outstanding electrochemical performance of PrGO-IL.

The Ragone plot of a PrGO-IL based supercapacitor is provided in Fig. 5c; it is clearly observed that the energy density does not show a significant drop with the increase of the power density, which is in good agreement with its good capacitance retention at high changing/discharge rates.[24] The maximum energy density of 7.0 W h kg^{-1} (with a power density of 0.5 kW kg^{-1}) and a power density of 13.3 kW kg^{-1} (with an energy density of 2.4 W h kg^{-1}) were obtained in aqueous 1 M H_2SO_4 electrolyte for 1 V window voltage. More importantly, these values are superior to the similar previously reported symmetrical systems with aqueous electrolyte, including graphene/MnO_2 (6.8 W h kg^{-1} at a power density of 62 W kg^{-1}),[57] porous graphene (with the largest energy density of 6.5 W h kg^{-1}),[24] GMCS composite (5.5 W h kg^{-1} at a power density of 50 W kg^{-1})[13] and DEG/graphene composite (with the maximum power density of 1.93 kW kg^{-1}).[21] Actually, the energy density could also be significantly improved by using an asymmetrical supercapacitor design[58] or choosing organic electrolytes to increases the operating voltage.[31]

To evaluate the feasibility and stability of our assembled device, we measured CV curves under the normal and bent states at the scan rate of 50 mV s^{-1}. The bent device is presented in Fig. 5d (inset). Interestingly, there is no significant difference between the CV curves before and after bending (Fig. 5d), confirming the outstanding mechanical flexibility. Continuously, the performance durability of the flexible device was further tested under bent states up to 1000 cycles. As expected, there is negligible variation in the CV curves, indicating its excellent mechanical and flexible properties.

Furthermore, we also connected two supercapacitor units in series to further demonstrate the practical usage of the PrGO-IL supercapacitor. Fig. 5e shows the corresponding GCD curves at current density of 4 A g^{-1} in different voltage ranges, which reveal nearly linear and symmetric charge/discharge profiles. More strikingly, after charging at 4 A g^{-1} with the voltage up to 1.5 V, it can successfully light the red light-

emitting-diode (LED) and continuously power it for about 10 min. The brightness change is presented in Fig. 5f. These impressive results again prove the great potential of PrGO-IL for electrochemical energy storage devices.

4. Conclusions

In summary, we have successfully demonstrated a dual "spacers"-assisted strategy for the preparation of functionalized 3D porous graphene (PrGO-IL) by low temperature hydrothermal method. In this synthesis, IL as a "spacer" plays important roles in building the unique 3D architecture and effectively suppressing the re-stacking of graphene. The introduction of SiO_2 spheres as another "spacer" can offer open macropores into the multilayer structure and further increase the specific surface area. These facilitate the diffusion and transport of electrolyte ions as well as benefit the rapid charge propagation during the charge–discharge process. Moreover, the designed strategy also allows the preservation of numerous stable oxygen-containing functionalities on graphene surface. They not only contribute pseudocapacitance to the entire composite electrode, but also significantly improve the accessibility of electrolytes to electrodes. Due to the synergistic effect of aforementioned features, the PrGO-IL exhibits high specific capacity of 262 F g^{-1} at 0.5 A g^{-1}, enhanced rate performance and excellent cycle stability in 1 M H_2SO_4 electrolyte. Particularly, the remarkable electrochemical performance was well maintained in symmetrical two-electrode device with the power density up to 13.3 kW kg^{-1}. More importantly, the generalized and rational method described here could inspire more novel designs of hierarchical and functional materials based on graphene for diverse practical usages such as sensors, catalysis and electronics devices.

Acknowledgements

The authors gratefully acknowledge the financial support for this research from the National Natural Science Foundation of China (21375043, 21175051).

Notes and references

1 J. R. Miller and P. Simon, *Science*, 2008, **321**, 651–652.
2 P. Simon and Y. Gogotsi, *Nat. Mater.*, 2008, **7**, 845–854.
3 G. Wang, L. Zhang and J. Zhang, *Chem. Soc. Rev.*, 2012, **41**, 797–828.
4 L. L. Zhang and X. S. Zhao, *Chem. Soc. Rev.*, 2009, **38**, 2520–2531.
5 D. Kong, J. Luo, Y. Wang, W. Ren, T. Yu, Y. Luo, Y. Yang and C. Cheng, *Adv. Funct. Mater.*, 2014, **24**, 3815–3826.
6 J. Zhang, Y. Yu, L. Liu and Y. Wu, *Nanoscale*, 2013, **5**, 3052–3057.
7 Z. Lei, L. Lu and X. S. Zhao, *Energy Environ. Sci.*, 2012, **5**, 6391–6399.
8 Y. Zhu, S. Murali, M. D. Stoller, K. J. Ganesh, W. Cai, P. J. Ferreira, A. Pirkle, R. M. Wallace, K. A. Cychosz, M. Thommes, D. Su, E. A. Stach and R. S. Ruoff, *Science*, 2011, **332**, 1537–1541.
9 C. Zhu, J. Zhai and S. Dong, *Nanoscale*, 2014, **6**, 10077–10083.
10 S. Giri, D. Ghosh and C. K. Das, *Adv. Funct. Mater.*, 2014, **24**, 1312–1324.
11 J. Yan, Q. Wang, T. Wei, L. Jiang, M. Zhang, X. Jing and Z. Fan, *ACS Nano*, 2014, **8**, 4720–4729.
12 K. Zhang, L. Mao, L. L. Zhang, H. S. O. Chan, X. S. Zhao and J. Wu, *J. Mater. Chem.*, 2011, **21**, 7302–7307.
13 Z. Lei, N. Christov and X. S. Zhao, *Energy Environ. Sci.*, 2011, **4**, 1866–1873.
14 Y. Meng, K. Wang, Y. Zhang and Z. Wei, *Adv. Mater.*, 2013, **25**, 6985–6990.
15 X. Wang, Y. Zhang, C. Zhi, X. Wang, D. Tang, Y. Xu, Q. Weng, X. Jiang, M. Mitome, D. Golberg and Y. Bando, *Nat. Commun.*, 2013, **4**, 2905.
16 S. Pei and H.-M. Cheng, *Carbon*, 2012, **50**, 3210–3228.
17 D. Yu, L. Wei, W. Jiang, H. Wang, B. Sun, Q. Zhang, K. Goh, R. Si and Y. Chen, *Nanoscale*, 2013, **5**, 3457–3464.
18 Y. Xu, K. Sheng, C. Li and G. Shi, *ACS Nano*, 2010, **4**, 4324–4330.
19 H. Zhang, T. Kuila, N. H. Kim, D. S. Yu and J. H. Lee, *Carbon*, 2014, **69**, 66–78.
20 B. You, L. Wang, L. Yao and J. Yang, *Chem. Commun.*, 2013, **49**, 5016–5018.
21 Y. Yu, Y. Sun, C. Cao, S. Yang, H. Liu, P. Li, P. Huang and W. Song, *J. Mater. Chem. A*, 2014, **2**, 7706–7710.
22 Z. Fan, Q. Zhao, T. Li, J. Yan, Y. Ren, J. Feng and T. Wei, *Carbon*, 2012, **50**, 1699–1703.
23 L. Jiang and Z. Fan, *Nanoscale*, 2014, **6**, 1922–1945.
24 H. Wang, X. Sun, Z. Liu and Z. Lei, *Nanoscale*, 2014, **6**, 6577–6584.
25 Z. Wen, X. Wang, S. Mao, Z. Bo, H. Kim, S. Cui, G. Lu, X. Feng and J. Chen, *Adv. Mater.*, 2012, **24**, 5610–5616.
26 X. Yang, J. Zhu, L. Qiu and D. Li, *Adv. Mater.*, 2011, **23**, 2833–2838.
27 C.-M. Chen, Q. Zhang, C.-H. Huang, X.-C. Zhao, B.-S. Zhang, Q.-Q. Kong, M.-Z. Wang, Y.-G. Yang, R. Cai and D.-S. Su, *Chem. Commun.*, 2012, **48**, 7149–7151.
28 Q. Wu, Y. Xu, Z. Yao, A. Liu and G. Shi, *ACS Nano*, 2010, **4**, 1963–1970.
29 Y. Yan, T. Kuila, N. H. Kim, B.-C. Ku and J. H. Lee, *J. Mater. Chem. A*, 2013, **1**, 5892–5901.
30 C. Zheng, X. Zhou, H. Cao, G. Wang and Z. Liu, *J. Power Sources*, 2014, **258**, 290–296.
31 Z. Lei, Z. Liu, H. Wang, X. Sun, L. Lu and X. S. Zhao, *J. Mater. Chem. A*, 2013, **1**, 2313–2321.
32 D.-C. Guo, J. Mi, G.-P. Hao, W. Dong, G. Xing, W.-C. Li and A.-H. Lu, *Energy Environ. Sci.*, 2013, **6**, 652–659.
33 W. S. Hummers Jr. and R. E. Offeman, *J. Am. Chem. Soc.*, 1958, **80**, 1339–1339.
34 Y. Cheng, H. Zhang, C. V. Varanasi and J. Liu, *Energy Environ. Sci.*, 2013, **6**, 3314–3321.

35 J. Zhang and X. S. Zhao, *J. Phys. Chem. C*, 2012, **116**, 5420–5426.
36 Z. Bo, W. Zhu, W. Ma, Z. Wen, X. Shuai, J. Chen, J. Yan, Z. Wang, K. Cen and X. Feng, *Adv. Mater.*, 2013, **25**, 5799–5806.
37 W. Zhou, X. Cao, Z. Zeng, W. Shi, Y. Zhu, Q. Yan, H. Liu, J. Wang and H. Zhang, *Energy Environ. Sci.*, 2013, **6**, 2216–2221.
38 H. Feng, R. Cheng, X. Zhao, X. Duan and J. Li, *Nat. Commun.*, 2013, **4**, 1539–1545.
39 A. C. Ferrari and J. Robertson, *Phys. Rev. B: Condens. Matter*, 2000, **61**, 14095–14107.
40 Z. H. Ni, H. M. Wang, Y. Ma, J. Kasim, Y. H. Wu and Z. X. Shen, *ACS Nano*, 2008, **2**, 1033–1039.
41 M. S. Dresselhaus, A. Jorio, M. Hofmann, G. Dresselhaus and R. Saito, *Nano Lett.*, 2010, **10**, 751–758.
42 L.-L. Li, K.-P. Liu, G.-H. Yang, C.-M. Wang, J.-R. Zhang and J.-J. Zhu, *Adv. Funct. Mater.*, 2011, **21**, 869–878.
43 W. Chen, L. Yan and P. R. Bangal, *Carbon*, 2010, **48**, 1146–1152.
44 H.-L. Guo, X.-F. Wang, Q.-Y. Qian, F.-B. Wang and X.-H. Xia, *ACS Nano*, 2009, **3**, 2653–2659.
45 S. Wang, D. Yu, L. Dai, D. W. Chang and J.-B. Baek, *ACS Nano*, 2011, **5**, 6202–6209.
46 Y. S. Lee, T. H. Cho, B. K. Lee, J. S. Rho, K. H. An and Y. H. Lee, *J. Fluorine Chem.*, 2003, **120**, 99–104.
47 Z. Wang, J. Wang, Z. Li, P. Gong, X. Liu, L. Zhang, J. Ren, H. Wang and S. Yang, *Carbon*, 2012, **50**, 5403–5410.
48 W. He, H. Jiang, Y. Zhou, S. Yang, X. Xue, Z. Zou, X. Zhang, D. L. Akins and H. Yang, *Carbon*, 2012, **50**, 265–274.
49 T. Kim, H. C. Kang, T. T. Tung, J. D. Lee, H. Kim, W. S. Yang, H. G. Yoon and K. S. Suh, *RSC Adv.*, 2012, **2**, 8808–8812.
50 N. Liu, F. Luo, H. Wu, Y. Liu, C. Zhang and J. Chen, *Adv. Funct. Mater.*, 2008, **18**, 1518–1525.
51 S. Wang, X. Wang and S. P. Jiang, *Phys. Chem. Chem. Phys.*, 2011, **13**, 6883–6891.
52 P. Gong, Z. Wang, J. Wang, H. Wang, Z. Li, Z. Fan, Y. Xu, X. Han and S. Yang, *J. Mater. Chem.*, 2012, **22**, 16950–16956.
53 Q. Wang, J. Yan, Y. Wang, G. Ning, Z. Fan, T. Wei, J. Cheng, M. Zhang and X. Jing, *Carbon*, 2013, **52**, 209–218.
54 U. M. Patil, K. V. Gurav, V. J. Fulari, C. D. Lokhande and O. S. Joo, *J. Power Sources*, 2009, **188**, 338–342.
55 F. Liu, S. Song, D. Xue and H. Zhang, *Adv. Mater.*, 2012, **24**, 1089–1094.
56 Z. Li, L. Zhang, B. S. Amirkhiz, X. Tan, Z. Xu, H. Wang, B. C. Olsen, C. M. B. Holt and D. Mitlin, *Adv. Energy Mater.*, 2012, **2**, 431–437.
57 Y. He, W. Chen, X. Li, Z. Zhang, J. Fu, C. Zhao and E. Xie, *ACS Nano*, 2013, **7**, 174–182.
58 Y. Cheng, H. Zhang, S. Lu, C. V. Varanasi and J. Liu, *Nanoscale*, 2013, **5**, 1067–1073.